Limited-Angle Computed Tomography for Sandwich Structures using Data Fusion

Jeffrey E. Boyd
Defence Research Establishment Pacific
FMO Victoria, BC, Canada, V0S 1B0

ABSTRACT

Both conventional and limited-angle computed-tomography (CT) are ill-posed problems, but where conventional CT has a small null space with few dimensions, limited-angle CT has a much larger null space and is severely ill-posed. The nature of the ill-posedness of limited-angle CT dictates that any limited-angle reconstruction method must interpolate from partial data in the Fourier domain. Large aluminum-core sandwich structures, such as those of aircraft control surfaces, simultaneously prevent full range data acquisition for CT and have face sheets that lie primarily in the limited-angle Radon transform null space. Consequently, interpolation of missing data is not possible and limited-angle CT for large sandwich structures is not feasible. This paper presents a novel method for limited-angle CT that addresses this problem. The method uses constraint-based data fusion to reduce the null space of the problem in a manner consistent with the specimen. Measurements of spatial support and face sheet thickness provide data for the additional constraints. By using the method, accurate reconstruction of sandwich structures becomes possible, where it would otherwise be impossible. The method of convex projections solves the inverse problem posed by the fusion system well because it is fast (for this problem) and easily incorporates the fusion constraints. Experimental results based on synthetic data show the improvement in reconstruction accuracy obtained by the fusion method. Real data results show the successful application of the method to a plexiglass phantom.

1. INTRODUCTION

This paper presents a novel method for limited-angle computed tomography (CT) that addresses the failure of current methods to accurately reconstruct sandwich structures. The method uses data fusion to apply additional constraints to the ill-posed problem of reconstruction. While general *a priori* assumptions used as constraints are sufficient to allow solution of the problem, such assumptions do not necessarily lead to accurate reconstructions. On the other hand, constraints provided by the data fusion constrain the solution in a manner consistent with the specimen and avoid inaccuracies associated with generalized assumptions.

Let $\mu(x,y)$ be the x-ray linear attenuation cross section of a specimen. The Radon transform of the cross section, $[\mathrm{R}\,\mu](l,\theta)$, is:

$$[\mathrm{R}\,\mu](l,\theta) = \int_{-\infty}^{\infty} \mu(l\cos\theta + \xi\sin\theta, \xi\cos\theta + l\sin\theta)d\xi. \tag{1}$$

The integral on the right-hand side of Eq. (1) is the ray sum of $\mu(x,y)$ for a ray at distance l from the origin and at angle θ to the y axis, and may be measured using an x-ray system. The complete Radon transform requires ray sums for θ throughout a range of π radians, i.e., $-\frac{\pi}{2} \le \theta < \frac{\pi}{2}$. Computed tomography (CT) is the inverse problem of reconstructing $\mu(x,y)$ from $[\mathrm{R}\,\mu](l,\theta)$. The reconstruction problem is ill-posed; in the continuous case the solution does not depend continuously on the data and in the discrete case the solution, if it exists, is not unique. In the latter case, the null space consists of high-frequency oscillations, and the *a priori* assumption that the solution is band-limited is sufficient to allow reconstruction (1).

Some objects or their environments, prevent acquisition of ray sum data throughout $-\frac{\pi}{2} \le \theta < \frac{\pi}{2}$, resulting in a limited-angle sampling of the Radon transform. Reconstruction from such data, referred to as limited-angle CT, is also ill-posed, but more so than for full-range data (2,3) (We say a problem is more ill-posed than another when it has a larger null space, i.e., a grater number of dimensions in its null space). The limited-angle Radon transform has a large null space as a result of incomplete sampling of the Fourier space.

Sandwich structures are commonplace and, by nature, often restrict ray sum acquisition to limited angles. For example, if the structure is wide, as is the case for aircraft components, it does not allow full range ray sum data acquisition. Furthermore, the face sheets of the sandwich lie almost entirely in the limited-angle Radon transform null space. The existence of key structural components in the null space invalidates assumptions necessary for the interpolation of the unsampled Fourier domain. Therefore, the nature of large sandwich structures confounds attempts at CT because of the limited-angle restriction and the unavoidable existence of the face sheets in the null space.

The method presented here solves limited-angle CT for wide sandwich structures. The system fuses spatial support and face sheet thickness data in a constraint-based data fusion system [(4)]. The additional data sources complement the ray sum data so that, as constraints, they reduce the null-space of the ensuing inverse problem. Not only does the fusion reduce the size of the null space, but because the constraints are based on actual measurements and not on erroneous *a priori* assumptions, the null space reduction is consistent with the specimen and the reconstruction is accurate [(5)].

2. LIMITED-ANGLE CT AND SANDWICH STRUCTURES

The limited-angle CT method described in this paper allows reconstruction of sandwich structures from limited-angle ray sum data. To understand the significance of the method, one must first consider the ill-posed nature of limited-angle CT and its implications regarding sandwich structures. To that end, this section first describes the source of ill-posedness in limited-angle CT and then shows how that ill-posedness confounds reconstruction where face sheets are present.

The Fourier slice theorem relates sampling with ray sums to sampling in the Fourier domain. Specifically, it states that the Fourier transform of the Radon transform for θ constant is identical to a slice in the Fourier domain, through the origin perpendicular to θ [(1,6)], i.e.:

$$[\mathrm{F}_l R\,\mu](\omega_l,\theta) = [\mathrm{F}_{x,y}\mu](\omega_l\cos\theta, -\omega_l\sin\theta), \tag{2}$$

where F_l is the one-dimensional Fourier transform operator in l, ω_l and θ are polar coordinates of the two-dimensional Fourier space, and $\mathrm{F}_{x,y}$ is the two-dimensional Fourier transform operator in Cartesian coordinates.

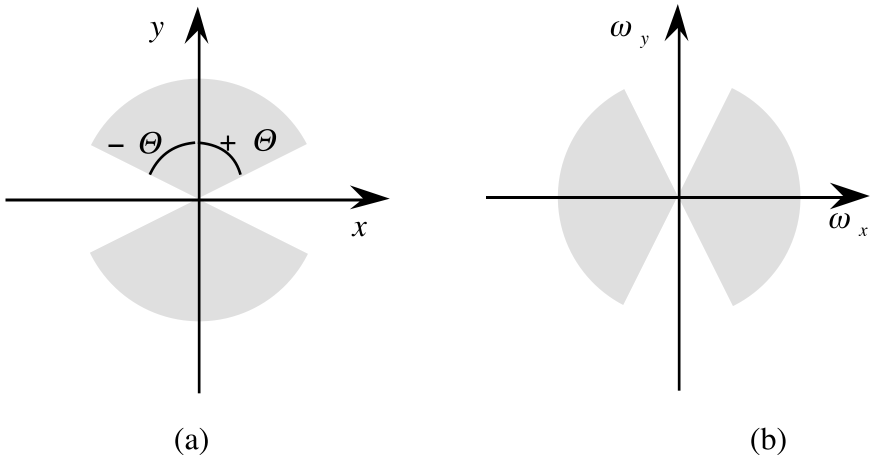

Fig. 1: Effect of limited-angle Radon transform on Fourier domain sampling: (a) range of angles sampled (shaded region) and (b) effective sampling of Fourier domain (shaded region is sampled).

Conventional CT reconstructs a cross section using ray sums throughout $-\frac{\pi}{2} \leq \theta < \frac{\pi}{2}$, and therefore uses a discrete sampling of the entire Radon transform. Limited-angle CT arises when an object or its environment restricts the range of θ, i.e., $-\Theta \leq \theta < \Theta$ where $\Theta < \frac{\pi}{2}$. In this case only the limited-angle Radon transform, $[\mathrm{R}_\Theta \mu](l, \theta)$, is available. The restriction on θ corresponds to a restriction on the sampling of the Fourier domain as shown in Fig. 1. Figure 1a shows the range of angles for θ, while Fig. 1(b) shows the corresponding sampling of the Fourier domain. Incomplete sampling of the Fourier domain forces any limited-angle CT method to determine what values should fill the unsampled region. Among the possibilities are filling with zeros (the minimum-norm solution [7]), interpolation subject to spatial constraints [8,9,6,10], and direct interpolation in the Fourier domain [11,12]. As always, interpolation requires *a priori* assumptions about the nature of the solution. The accuracy of the reconstruction depends upon the validity of those assumptions, i.e., erroneous assumptions lead to inaccurate reconstructions.

If a component of the specimen is in the null space of the limited-angle Radon transform, then, by definition, the ray sum data do not reflect its presence. For limited-angle CT, the null space is the set of all functions whose value is zero inside the region of the Fourier domain sampled by the limited-angle transform, i.e.:

$$\mathrm{N}\,(\mathrm{R}_\Theta) = \left\{ \mu_n(x,y) \colon \begin{array}{l} [\mathrm{F}_{x,y}\,\mu_n](\omega_x,\omega_y) = 0,\, -\Theta \le \theta \le \Theta, \\ \tan\theta = \dfrac{\omega_y}{\omega_x},\ [\mathrm{F}_{x,y}\,\mu_n](0,0) = 0 \end{array} \right\}, \tag{3}$$

where $\mathrm{N}\,()$ denotes null space. Because null space components are invisible to the ray sum data, there is no basis for accurate interpolation and the presence of such components confounds accurate reconstruction [13,5].

Sandwich structures, such as the graphite/epoxy and aluminum honeycomb control surfaces of some aircraft, are an important example of structures that contain null space components. If the structure is wide, as is the case for aircraft control surfaces, it does not allow full range ray sum data, and furthermore, the face sheet structure lies almost entirely in the limited-angle Radon transform null space. Figure 2 illustrates this fact. Let the function $s_{r,\phi,a,d}(x,y)$, illustrated in Fig. 2b, to represent a face sheet, where $s_{r,\phi,a,d}(x,y)$ is given by:

$$s_{r,\phi,a,d}(x,y) = \begin{cases} a, & -\dfrac{\mathrm{d}}{2} \le (x\sin\phi + y\cos\phi) - r \le \dfrac{d}{2}, \\ 0, & \text{otherwise} \end{cases} \tag{4}$$

i.e., a rectangular function in the y-axis direction with amplitude a, width d, distance r from the origin, and oriented at angle ϕ to the y axis. The Fourier transform of $s_{r,\phi,a,d}(x,y)$ is:

$$[\mathrm{F}_{x,y}s_{r,\phi,a,d}](\omega_x,\omega_y) = \delta(\omega'_x)ad\,\mathrm{sinc}(\pi d\omega'_y)e^{-j\omega'_y r}, \tag{5a}$$

where

$$\begin{bmatrix}\omega'_x \\ \omega'_y\end{bmatrix} = \begin{bmatrix}\cos\phi & -\sin\phi \\ \sin\phi & \cos\phi\end{bmatrix}\begin{bmatrix}\omega_x \\ \omega_y\end{bmatrix}, \tag{5b}$$

i.e., the Fourier transform is a sinc function along the y axis, phase shifted (for r) and rotated by angle ϕ. Figure 2b shows a sandwich structure with two face sheets surrounding some core material. The width of the structure restricts the range of angles to $-\Theta \le \theta \le \Theta$ where $\Theta < \dfrac{\pi}{2} - \phi$. Thus, with the exception of the zero-frequency components, the face sheets lie within the null space of the limited-angle Radon transform. The presence of the face sheets confounds reconstruction and their existence in the null space prevents the possibility of accurate reconstruction based on general *a priori* assumptions. There is no valid basis for interpolation for such a specimen.

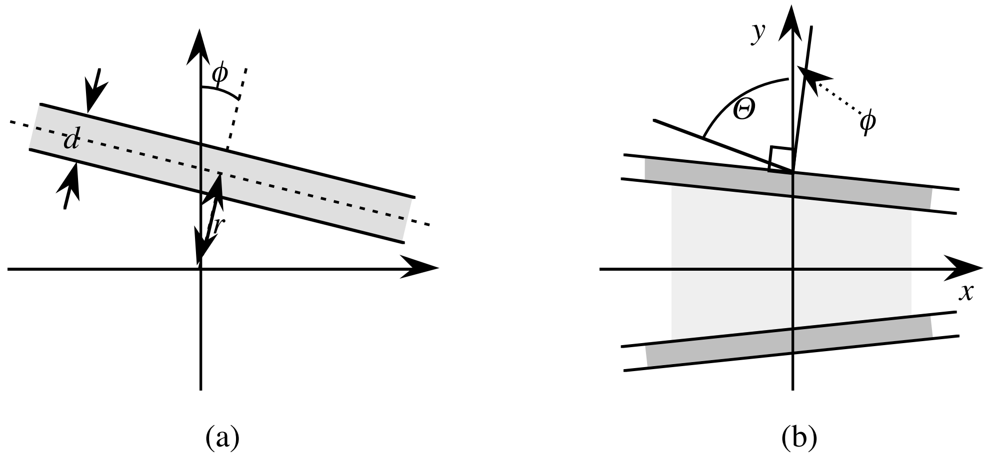

Fig. 2: Face sheets in a sandwich structure: (a) the function $s_{r,\phi,a,d}(x,y)$; (shaded region has value a and zero everywhere else) models the face sheets, and (b) a sandwich specimen with face sheets at angle ϕ. The width of the specimen prevents ray sum acquisition outside the range $-\Theta \leq \theta \leq \Theta$. Note that $\Theta < \frac{\pi}{2} - \phi$ so the face sheets lie almost entirely within the limited-angle Radon transform null space.

3. A NOVEL DATA FUSION SYSTEM FOR LIMITED-ANGLE CT

Clearly, limited-angle CT for sandwich structures using only ray sum data is not feasible. The face sheets of the sandwich lie in the limited-angle Radon transform null space rendering assumptions necessary for interpolation invalid. In order for limited-angle CT to be successful, it must properly account for the null space.

We now describe a novel system for limited-angle CT that deals with the limited-angle Radon transform null space. The system uses constraint-based data fusion [4] to solve the ill-posed reconstruction problem. Whereas current limited-angle methods rely on *a priori* assumptions to constrain the problem and arrive at a unique solution, constraint-based data fusion uses data from other sources to provide constraints and avoids problems that arise when assumptions are not valid. It is not sufficient to simply employ data fusion; the data sources must be complementary (i.e., each data source provides unique information) so that the added constraints reduce the null space [5]. The novel system described here uses complementary data sources to reduce the null space in a manner consistent with the specimen. In doing so, the system produces accurate tomographic reconstructions of sandwich structures where it would otherwise be impossible.

3.1. Data Acquisition

CT requires a carefully arranged set of ray sums that sample the Radon transform of the specimen. Figure 3 shows the motion of a hypothetical apparatus during ray sum acquisition. The system acquires a set of parallel ray sums by scanning the specimen along a line. Initially, the projection angle (the angle between vertical and the source-sensor plane) is zero (Fig. 3a). Subsequent scans acquire projection data for angles in the range $-\Theta \leq \theta \leq \Theta$ (Fig. 3b).

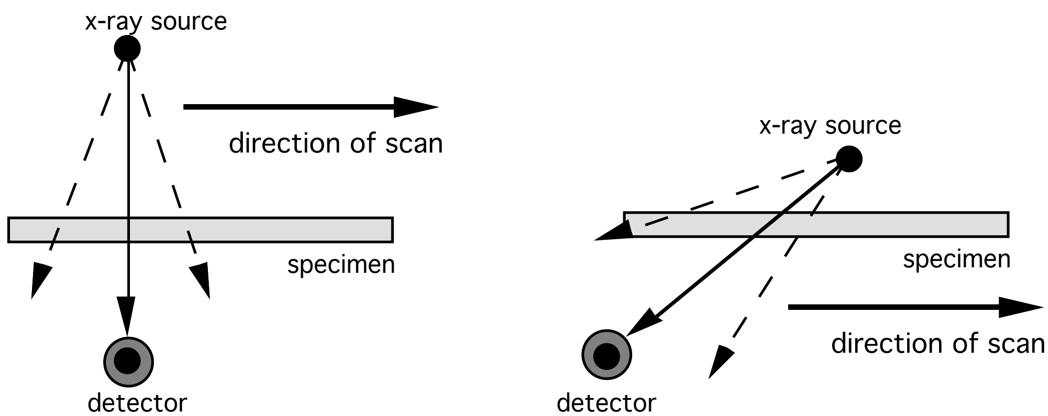

(a) (b)

Fig. 3: Scan method for limited-angle ray sum acquisition: (a) parallel with vertical and (b) at an angle to vertical.

The CT system described here uses two sources of data in addition to the ray sums: spatial support data and face sheet thickness data. Measuring spatial support is equivalent to locating the upper and lower surfaces of the specimen. A variety of means is available for this measurement. For example, Fig. 4 shows two laser range finders situated beside the x-ray source and detector. Each laser range finder projects a small dot of laser light onto the surface of the specimen. The optical system of the range finder detects the dot and triangulates its position. By sweeping the dot along a line and triangulating at each position, the range finder acquires range data along a line. To collect range data over an area, the range finder sweeps across the area. Only the center of the scan is necessary for reconstruction of the cross section.

A less expensive alternative to laser range finders is to use a variation of stereo vision. In the stereo system, two video cameras mounted in place of the range finders acquire a sequence of images as the apparatus sweeps across the specimen. From these images, it is possible to compute range data, i.e., compute depth from motion, where the motion is known.

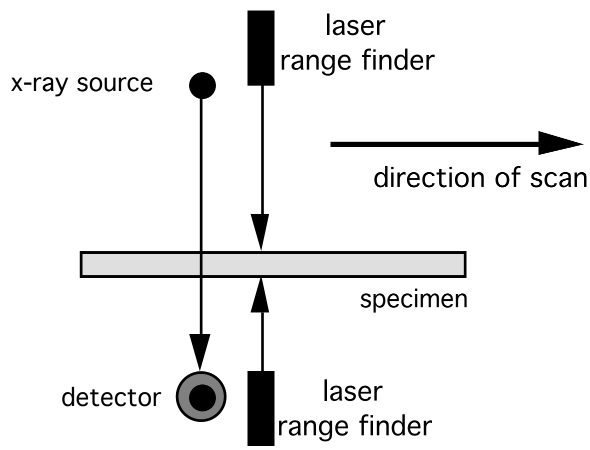

Fig. 4: Scanning method modified to include laser range finder for spatial support measurement.

Face sheet thickness data are also available from a variety of sources. Figure 5 shows a pulse-echo ultrasound system for thickness measurement. Two separate transducers measure the thicknesses of the upper and lower face sheets. To acquire data for the region of reconstruction, the ultrasound system scans along a line in the same manner as the ray sum and spatial support measurement systems. Ideally, the pulse-echo traces have two reflections, one from the outer surface and one from the inner surface. The time delay between the two reflections gives the thickness at that point (assuming that the speed of sound is known). Conceptually, the ultrasound apparatus of Fig. 5 could be situated beside the x-ray system, but practical requirements for ultrasound (e.g., water squirters) and x-ray (high-voltage circuits) prohibit their coexistence. Therefore, the ultrasound apparatus is separate from the x-ray and range apparatus.

It is possible that the ultrasound thickness measurement may fail occasionally. This can occur for many reasons, e.g., scattering obstructions, defects within the face sheet, or internal structures that confound the reflections. Fortunately, the thickness of the face sheets is not rapidly varying and interpolation of missing thickness values is a straightforward process.

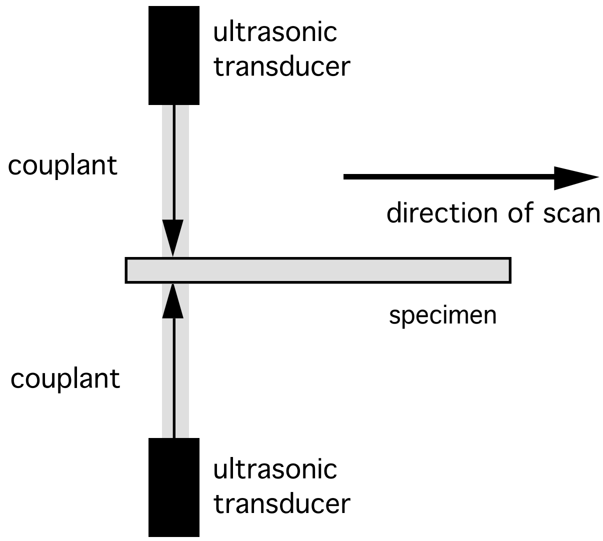

Fig. 5: Apparatus for ultrasound data acquisition.

Compton back scatter imaging provides an alternative means of measuring face sheet thickness by detecting back scattered radiation. The method is expensive and does not have the resolution of ultrasound, however the resolution is sufficient for the CT problem and the measurement is not confounded by factors that affect ultrasound.

As previously stated, it is necessary for the additional data sources to complement the ray sum data. This is indeed the case for the spatial support and face sheet thickness data with respect to the ray sum data. Ray sums are insensitive to discontinuities along the path of the radiation, so the limited-angle ray sum data cannot locate the positions of the face sheets. On the other hand, the spatial support and face sheet thickness data precisely locate the discontinuities that delineate the face sheets, so the data sources are complementary. This complementary nature leads to a reduction in null space that is consistent with the specimen.

3.2. The Fusion System

The constraint-based (or strongly-coupled) feed-forward data fusion system of Fig. 6 processes the data acquired by the apparatus of Figures 3 through 5. The system is composed of three modules, one for each of the three data sources: spatial support, face sheet thickness, and ray sum. Each module solves an inverse problem, although the problems for spatial support and face sheet thickness are simple.

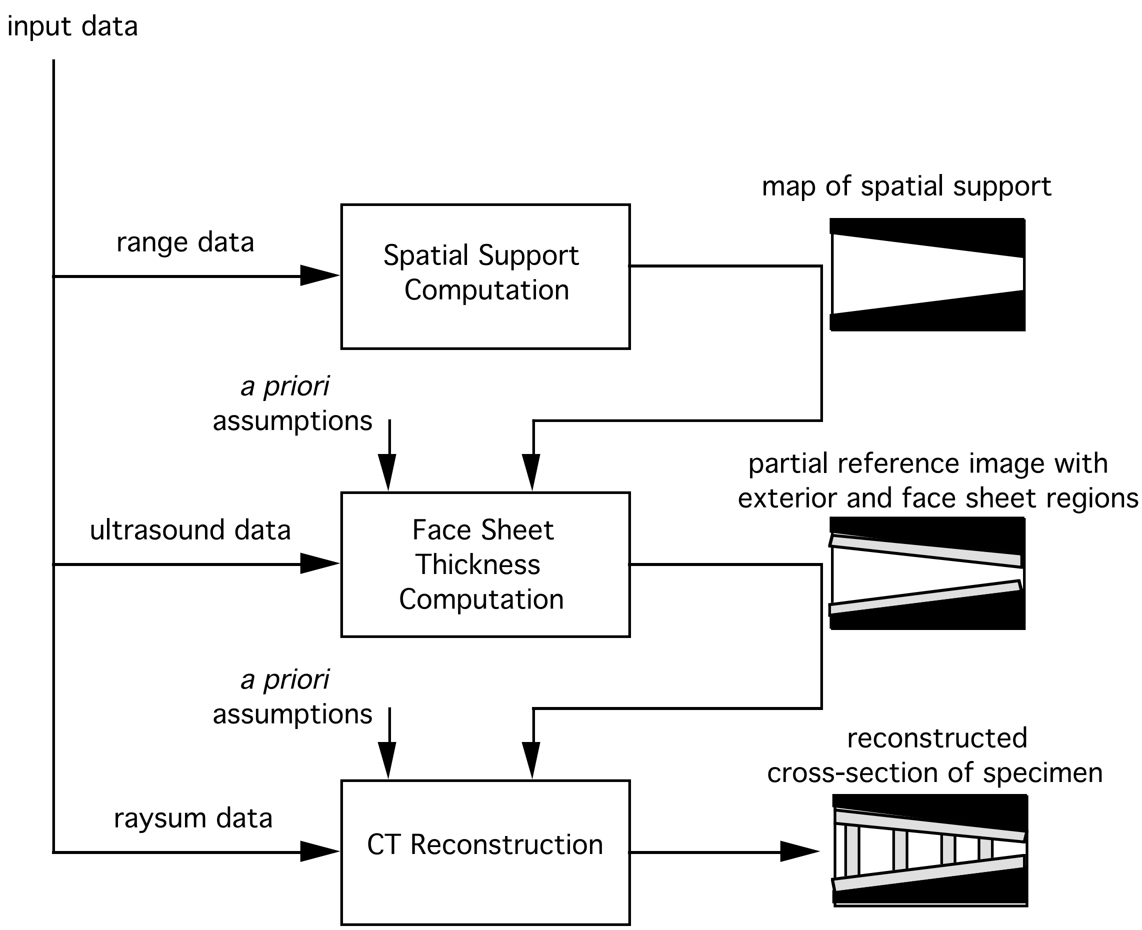

Fig. 6: Block diagram of strongly-coupled feed-forward data fusion system for limited-angle CT of sandwich structures.

The first module of the system, spatial support computation, takes range data (from a laser finder or equivalent) as input and produces a map of the spatial support for the specimen. The map segments the cross section into exterior regions and regions within the specimen.

The second module, face sheet thickness computation, takes face sheet thickness data (from ultrasound or equivalent) as input and computes a map that segments the specimen into exterior regions, face sheet regions, and interior regions. The thickness data, constrained by the spatial support data, define the positions of the face sheets. Combined, the face sheet positions and thickness give a map of the face sheet regions. Thus, the output of the face sheet module is a segmentation of the reconstruction into exterior, interior, and face sheet regions.

We know *a priori* that the specimen has zero linear attenuation in the exterior and the linear attenuation of the face sheet material can be measured. From this information and the segmentation output by the second module, one can build a partial reference image of the reconstruction containing the exterior and face sheet regions. The first two modules resolve no interior structure.

The third module, CT reconstruction, computes a cross section of the specimen from ray sums using the partial reference image from previous modules as a constraint. Because the data in the reference image complement the ray sum data, the ensuing reconstruction is accurate; the presence of the face sheets no longer confounds reconstruction.

3.3. Mathematical Formulation

The following linear system models ray sum acquisition of a piece-wise constant specimen:

$$R\mathbf{x} = \mathbf{y}\,, \tag{6}$$

where **x** is a vector of linear attenuation coefficients in a specimen and **y** is a vector of ray sums. R is a matrix representing the discrete Radon transform. Each ray sum measurement is given by the inner product:

$$y_i = \langle \mathbf{r}_i, \mathbf{x} \rangle\,, \tag{7}$$

where y_i is the i^{th} ray sum and $\mathbf{r}_i$ is the i^{th} row of R. The j^{th} element of $\mathbf{r}_i$, $r_{i,j}$, is the length of the i^{th} ray that passes through the j^{th} element of **x**. For limited-angle ray sum acquisition, R contains only those rows corresponding to ray sums that are possible to measure. The available ray sums determine R and the number of singular values equal to zero that it has. From Section 2 we know that R has a non-trivial null space containing the face sheet structures with the exception of the zero frequency component (or mean value). Therefore, accurate CT reconstruction based on Eq. (6) alone is intractable.

Range data and ultrasound data provide additional constraints to allow recovery of the face sheet structure. The segmentation based on the range and ultrasound data lead to the following system of equations:

$$W\mathbf{x} = W\mathbf{x}_F \tag{8}$$

where:

$$W = \mathrm{diag}(w_1, w_2, \ldots, w_j, \ldots, w_N) \quad ,$$

$$w_j = \begin{cases} 1 & x_j \text{ in face sheet or exterior} \\ 0 & x_j \text{ in specimen interior} \end{cases} \quad , \text{ and}$$

$$x_{F_j} = \begin{cases} \mu_{\text{air}} & x_j \text{ outside specimen} \\ \mu_{\text{fs}} & x_j \text{ in face sheet} \\ 0 & x_j \text{ in specimen interior} \end{cases} \quad .$$

The subscript F denotes fusion. $\mu_{\text{air}} = 0$ is the linear attenuation coefficient for air and μ_{fs} is the linear attenuation coefficient of the face sheet material. $\mathbf{x}_F$ is a partial reference image based on the spatial support and face sheet thickness data. The segmentation from the first two modules gives the elements on the diagonal of W. Intermediate values between zero and one on the diagonal indicate that a particular element lies across a boundary between regions.

Equations (6) and (8) combine to form the system:

$$\begin{bmatrix} R \\ W \end{bmatrix} \mathbf{x} = \begin{bmatrix} \mathbf{y} \\ W\mathbf{x}_F \end{bmatrix}. \tag{9}$$

Solving for $\mathbf{x}$ from Eq. (9) yields a solution that is constrained by Eq. (8) and therefore constrained by the spatial support and face sheet thickness data. Equation (9) eliminates the face sheet structures from the null space of $\begin{bmatrix} R \\ W \end{bmatrix}$, allowing a reconstruction that properly accounts for the face sheets.

Note that the null space is still non-trivial and the inverse problem is still ill-posed. The reconstruction still requires *a priori* assumptions, but these assumptions no longer lead to erroneous results. Wide internal structures with edges parallel or near parallel to the face sheets are still a problem. In practice, internal structures are much narrower than the face sheets so more of their Fourier transform lies in the sampled Fourier space, allowing better interpolation from *a priori* assumptions.

4. RECONSTRUCTION METHOD

Reconstruction by the fusion system requires solving for $\mathbf{x}$ from the linear system

$$A\mathbf{x} = \mathbf{b} \tag{10}$$

where:

$$A = \begin{bmatrix} R \\ W \end{bmatrix} \text{ and } \mathbf{b} = \begin{bmatrix} \mathbf{y} \\ W\mathbf{x}_F \end{bmatrix}.$$

The nature of A dictates that solving for $\mathbf{x}$ is an ill-posed problem; if a solution exists, it is not unique. A plethora of methods exists for such problems, but for this paper we consider only the method of convex projections (CP). CP is flexible, able to incorporate a variety of constraints. As such, it is particularly useful for constraint-based data fusion. Here we present a terse description of CP extracted from Brègman [14], Youla and Webb [15], Gubin *et al.* [16], and Bauschke and Borwein [17]. CP appears in other forms in CT literature, most notably ART (algebraic reconstruction technique) [18,1,19]. See Censor and Herman [18] for a review of projection methods, or Bauschke and Borwein [17] for a detailed survey.

CP assumes a set of m constraints on the domain of A, all of the form:

$$\mathbf{x} \in \mathrm{C}_i , \tag{11}$$

for $1 \le i \le m$, where C_i is a convex set. Combined, the constraints restrict the solution to lie in the convex set C_0, i.e.:

$$\mathbf{x} \in \mathrm{C}_0 = \bigcap_{i=1}^{m} \mathrm{C}_i . \tag{12}$$

POCS makes the important assumption that C_0 is non-empty. Each convex set C_i has a corresponding projection operator P_i of the form:

$$P_i \mathbf{z} = \begin{cases} \text{point in } C_i \text{ closest to } \mathbf{z}, & \mathbf{z} \notin C_i \\ \\ \mathbf{z}, & \text{otherwise} \end{cases} . \tag{13}$$

Application of P_i to some point $\mathbf{z}$ finds the point in C_i closest to $\mathbf{z}$. Points within C_i are fixed points of P_i.

The sequence $\{\mathbf{x}_n\} = \{P^n \mathbf{x}_0\}$ where $P = P_m P_{m-1} \ldots P_1$ converges weakly to a point in C_0. Furthermore, if $\mathbf{x}$ is in Euclidean space then the convergence is strong. In some circumstances the rate of convergence is linear. More generally, the sequence $\{\mathbf{x}_n\} = \{T^n \mathbf{x}_0\}$ where $T = T_m T_{m-1} \ldots T_1$, $T_i = 1 + \lambda_i (P_i - 1)$, and λ_i are relaxation coefficients in the range $0 \le \lambda_i \le 2$ exhibits the same convergence properties. However, in the context of this paper we use only non-relaxed operators, i.e., $\lambda_i = 1$ for all *i*.

If $\mathbf{x}_0 = \mathbf{0}$ then $P_0 \mathbf{x}_0$ is the minimum-norm solution, where P_0 is the projection onto the intersection C_0. However, CP does not compute $P_0 \mathbf{x}_0$, but only guarantees that it finds a solution that lies within C_0. The ultimate solution varies with the order of projection operators. If the minimum-norm property is essential, then one may use Hildreth's method (18) or Brègman's method (14,18).

Application of CP to the limited-angle CT problem with data fusion requires specification of convex constraints and corresponding projection operators. The flexibility of the method leads to diversity of constraint sets for CT. Three different constraint types are sufficient for the problem at hand. These are:

1. fit to ray sum data,
2. fit to range and ultrasound data, and
3. amplitude constraints.

Equation (6) forms the basis of the first constraint type. Consider each ray sum measurement, y_i, independently. Each measurement constrains the solution to lie within the hyperplane defined by:

$$\langle \mathbf{r}_i, \mathbf{x} \rangle - y_i = 0, \tag{14}$$

where $\mathbf{r}_i$ is the i^{th} row of R. Recognizing that the data are imperfect, we use the hyperslab centered about the hyperplane of Eq. (14) given by:

$$\mathcal{C}_{R_i} = \left\{ \mathbf{x} : \left| \langle \mathbf{r}_i, \mathbf{x} \rangle - y_i \right| \le \varepsilon_R \right\}, \tag{15}$$

where ε_R is the allowed margin for error in the fit to ray sum data and determines the thickness of the slab. Equation (15) breaks down into the two intersecting half planes:

$$\begin{aligned} \mathcal{C}_{R_{ia}} &= \left\{ \mathbf{x} : \langle \mathbf{r}_i, \mathbf{x} \rangle - y_i \le \varepsilon_R \right\} \\ \mathcal{C}_{R_{ib}} &= \left\{ \mathbf{x} : y_i - \langle \mathbf{r}_i, \mathbf{x} \rangle \le \varepsilon_R \right\} \end{aligned}. \tag{16}$$

The corresponding projection operators are:

$$P_{R_{ia}} \mathbf{z} = \begin{cases} \mathbf{z} + \dfrac{y_i + \varepsilon_R - \langle \mathbf{r}_i, \mathbf{z} \rangle}{\langle \mathbf{r}_i, \mathbf{r}_i \rangle} \mathbf{r}_i, & \langle \mathbf{r}_i, \mathbf{z} \rangle - y_i > \varepsilon_R \\ \mathbf{z}, & \text{otherwise} \end{cases}, \tag{17}$$

and

$$P_{R_{ib}} \mathbf{z} = \begin{cases} \mathbf{z} + \dfrac{y_i - \varepsilon_R - \langle \mathbf{r}_i, \mathbf{z} \rangle}{\langle \mathbf{r}_i, \mathbf{r}_i \rangle} \mathbf{r}_i, & y_i - \langle \mathbf{r}_i, \mathbf{z} \rangle > \varepsilon_R \\ \mathbf{z}, & \text{otherwise} \end{cases}. \tag{18}$$

The constraint sets of Eq. (15) allow control over the margin of error, ε_R, to vary the size of the sets and ensure that $\mathcal{C}_0$ is non-empty.

Fusion constraints originate from the linear system of Eq. (8). Oskoui-Fard and Stark[20] use a full reference image to constrain limited-angle CT. The concept is similar to the fusion problem here except that Oskoui-Fard and Stark assume a complete reference image, i.e., $W = I$, whereas we have a partial reference image. The partial reference image leads to the convex constraint set:

$$\mathcal{C}_F = \left\{ \mathbf{x} : \left\| W(\mathbf{x} - \mathbf{x}_F) \right\| \le \varepsilon_F \right\}, \tag{19}$$

with the corresponding projection operator:

$$P_F \mathbf{z} = \begin{cases} (I - W)\mathbf{z} + W\mathbf{x}_F + \varepsilon_F \dfrac{W(\mathbf{z} - \mathbf{x}_F)}{\left\| W(\mathbf{z} - \mathbf{x}_F) \right\|}, & \left\| W(\mathbf{z} - \mathbf{x}_F) \right\| > \varepsilon_F \\ \mathbf{z} & \text{otherwise} \end{cases}. \tag{20}$$

Amplitude constraints are the third and last constraint type. It is physically impossible to have a negative linear attenuation coefficient. Also, one can usually determine a maximum allowable linear attenuation based on knowledge of what materials are in the object. Therefore, the amplitude of a pixel in a reconstruction must lie between a lower and an upper bound, giving the following convex constraint sets:

$$C_{A_i} = \{\mathbf{x} : a \le x_i \le b, \quad 0 \le a < b\}, \tag{21}$$

where the subscript *A* refers to amplitude. The C_{A_i} are also hyperslabs and their corresponding projection operators are:

$$P_{A_i}\mathbf{z} = \begin{cases} \mathbf{z} : z_i = a & z_i < a \\ \mathbf{z} : z_i = b & z_i > b \\ \mathbf{z} & \text{otherwise} \end{cases}. \tag{22}$$

Amplitude constraints amount to simply clipping the data so that pixel values lie between the prescribed upper and lower bounds.

Limited-angle CT reconstruction using CP follows these steps:

1. set $\mathbf{x}_0 = \mathbf{0}$.
2. perform an iteration by computing:
$$\mathbf{x}_1 = P_{A_n} P_{A_{n-1}} \dots P_{A_1} P_F P_{R_m} P_{R_{m-1}} \dots P_{R_1} \mathbf{x}_0 .$$
3. repeat step 2 to compute the series $\{\mathbf{x}_n\} = \{P^n \mathbf{x}_0\}$ until convergence.

5. EXPERIMENTATION

Experiments described here use both synthetic and real data. Synthetic data demonstrates the effectiveness of the technique in the absence of noise and other confounding factors. Real data results show the practical application of the method. All computation is in single precision floating point.

5.1. X-ray Apparatus

The x-ray apparatus, shown schematically in Fig. 7, is intended for planar projection radiography. It sits on a large *C*-shaped manipulator ("*C*-arm") that allows the x-ray source and sensor (a linear array x-ray detector) to maneuver about a thin specimen. To acquire a radiographic image, the *C*-arm sweeps the array across an area, while a frame buffer assembles the image from the lines of data acquired by the array. Only a single x-ray detector is required for the tomography experiment described here, so only the center element of the array is used.

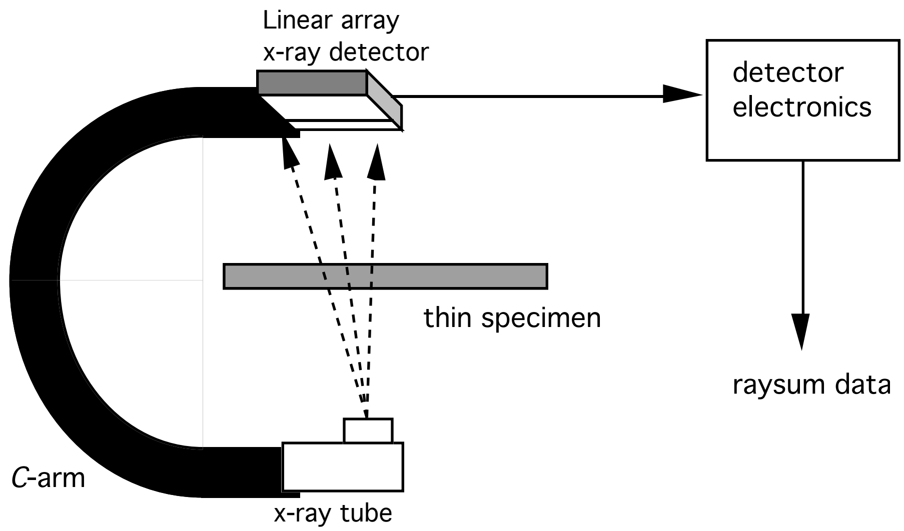

Fig. 7: Ray sum data acquisition system.

5.2. Implementation of Convex Projections

The method of convex projections (CP) requires a representation of the ray sum operator, *R*, for reconstruction. Each row of the operator is a vector in which each element is the distance an individual ray passes through an element of the reconstruction. The matrix required to represent all rows of the ray sum operator is huge (207,360,000 elements for the following 200 by 72 *pixel* example). However, most elements of each row are zero, i.e., *R* is sparse, and there are patterns in the operator that lead to a compact representation.

Figure 8a shows a hypothetical grid for reconstruction. Elements of the ray sum operator rows are the distances a particular ray travels through each box in the grid. A clipping algorithm (from computer graphics) computes these distances. Figure 8b shows the set of rays corresponding to a scan across the specimen parallel to vertical. A scan at an angle to vertical measures ray sums for the set of rays shown in Fig. 8c. Rays for a scan at a constant angle are parallel, and parallel ray sums are identical to each other except that the columns (of the reconstruction grid) are offset corresponding to the motion of the scan. This unconventional scanning geometry results in a situation where the spacing between rays varies with the angle of the rays. The varied spacing is not a problem because CP is flexible with respect to geometry, and this arrangement leads to an efficient implementation of the algorithm. With the exception of the column offsets, the set of rays in Fig. 8d, where there is one ray for each scan angle, completely describes all rays used in sampling. Therefore, to get a compact representation of the ray sum operator:

1. record only one row of the operator for each scan angle, and
2. record only non-zero elements.

The compact ray sum operator is a list of vectors with one element in the list for each scan angle. Each vector is a list of non-zero distances as well as the row and column coordinates for the corresponding grid elements. To recover quickly a non-zero element of a row in *R*:

1. select the vector for the appropriate angle from the compact representation, and
2. apply the appropriate column offset to the column coordinates of the vector.

R has one row for each combination of scan angle and column offset, but excludes those combinations that produce rays passing beyond the width of the reconstruction grid.

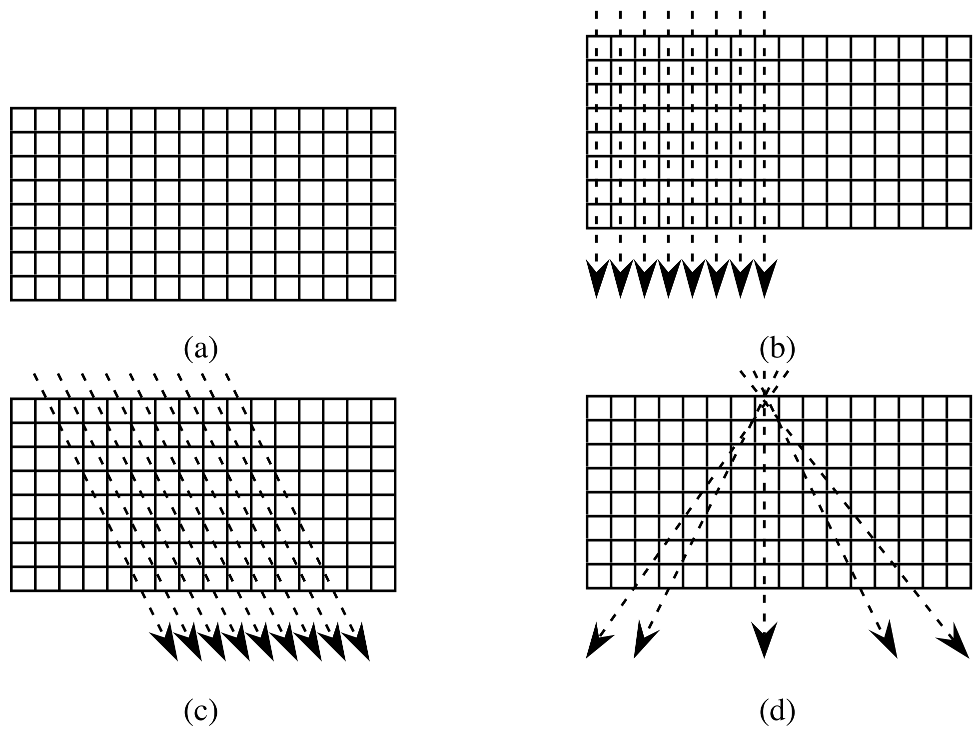

Fig. 8: Steps to a compact ray sum operator: (a) hypothetical grid for reconstruction, (b) parallel rays perpendicular to upper surface of reconstruction, (c) parallel rays and angle to reconstruction, and (d) set of rays, one at each scan angle.

CP computes the sequence $\{\mathbf{x}_n\} = \{P^n \mathbf{x}_0\}$, where $P = P_m, P_{m-1}, \ldots, P_1$ and P_i is the projection onto the i^{th} constraint set. Equations (17) and (18) give the two projection operators required for the first constraint type. The salient feature of these equations is the inner products $\langle \mathbf{r}_i, \mathbf{z} \rangle$ and $\langle \mathbf{r}_i, \mathbf{r}_i \rangle$. The compact ray sum operator allows fast computation of these inner products by allowing quick recovery of the non-zero elements of R. The second constraint type is the data fusion constraint. Computation of the projection for the fusion constraint is straight forward; it involves only computation of the inner products of vectors that are directly available. Implementation of the third constraint type, amplitude constraints, is trivial requiring only that all the elements of the solution to be clipped to lie within the specified upper and lower bounds.

It is important to specify starting and stopping conditions. Although CP does not generally compute the minimum-norm solution, these experiments use $\mathbf{x}_0 = \mathbf{0}$ in order to arrive at a solution near the minimum-norm solution. This starting condition does not guarantee such an outcome, but works well in practice. Iteration terminates when the norm $\|\mathbf{x}_i - \mathbf{x}_{i-1}\|$ falls below a specified level, i.e., the solution stops moving (or slows sufficiently). Note that this stopping condition does not guarantee that the solution is good, just that the solution is not going anywhere.

5.3. Synthetic Data Trials

We present three trials reconstructing a cross section from synthetic data from:

1. ray sum data only,
2. ray sum and spatial support data, and
3. ray sum, spatial support and face sheet data.

Generation of synthetic data starts with the cross section of Fig. 9 as the subject. Synthetic data in these experiments simulate the conditions of the plexiglass phantom used in the real data trial. The phantom mimics the basic structure of a graphite/epoxy and aluminum honeycomb sandwich with two plexiglass face sheets surrounding a set of vertical plexiglass members. All plexiglass parts are $3\,mm$ thick which, with a reconstruction resolution of $0.5\,mm$ by $0.5\,mm$, translates to 6 *pixels* thick in the reconstruction. On a reconstruction grid 72 *pixels* by 200 *pixels,* the reconstruction corresponds to a cross section $36\,mm$ thick by $100\,mm$ wide. Application of the ray sum operator to the image yields the ray sum data for the trials. For experiments presented here we use ray sums at angles from -60° to +60° with respect to vertical, in steps of 10°. The cross section also defines the spatial support data and the face sheet data directly. Figure 10 shows the fusion data: Figs. 10a and 10b are the diagonal of W and $\mathbf{x}_F$ respectively for spatial support data only, and Figs. 10c and 10d are the same for spatial support and face sheet data combined. For synthetic trials, the assumed linear attenuation of plexiglass is $0.40\,cm^{-1}$. The ray sum data are noise- and error-free.

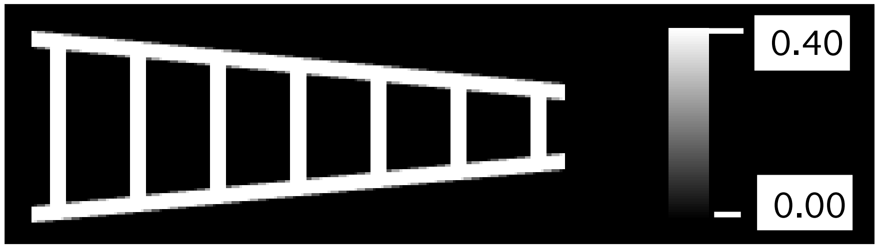

Fig. 9: Cross section for synthetic data trials.

Figure 11 shows the reconstructions for the three synthetic data trials. Table 1 summarizes the results. The error measure, e, given by [21]:

$$e = \frac{\|\mathbf{x} - \hat{\mathbf{x}}\|}{\|\mathbf{x}\|} \times 100\% \ ,$$

where $\mathbf{x}$ is the true cross section and $\hat{\mathbf{x}}$ is the reconstructed cross section, indicates the accuracy of reconstruction.

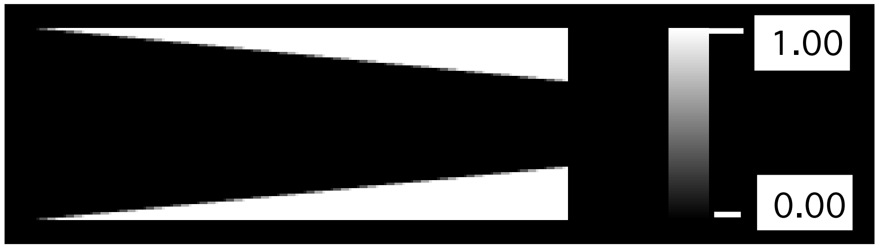

(a)

(b)

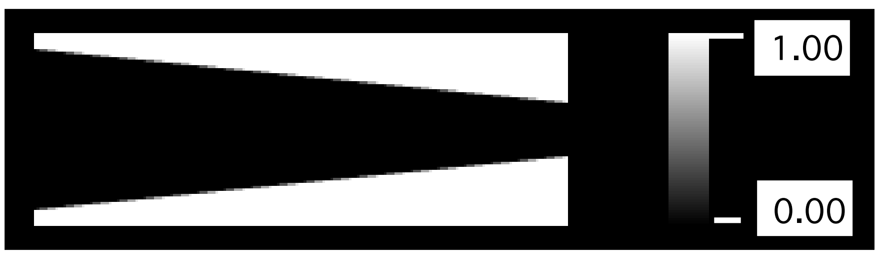

(c)

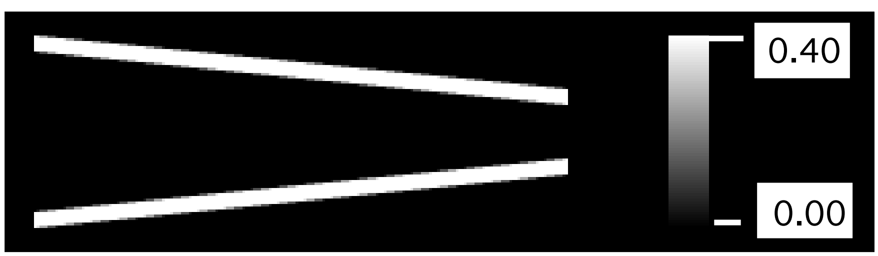

(d)

Fig. 10: Synthetic fusion data vectors: for spatial support data only (a) known region and (b) known linear attenuation, and for spatial support and face sheet data (c) known region and (d) known linear attenuation.

The trials exhibit a marked improvement in accuracy due to data fusion. While using no fusion data constraints yields an error measure of 62.6%, use of spatial support constraints reduces the error measure to 38.9%. Use of both spatial support and face sheet constraints further reduces the error to 6.0%. These results demonstrate the improvement in accuracy of limited-angle CT achieved by data fusion. The improvement arises because the fusion constraints reduce the size of the null-space of the problem in a manner consistent with the structure of the specimen.[13]

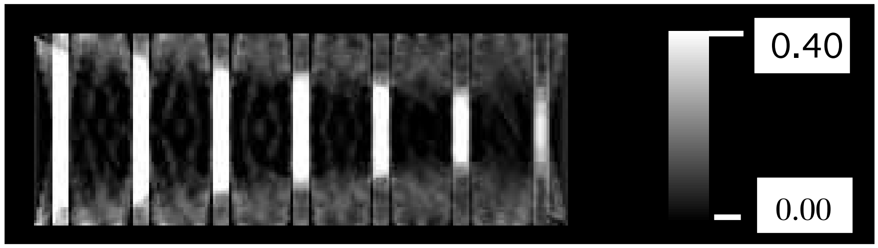

(a)

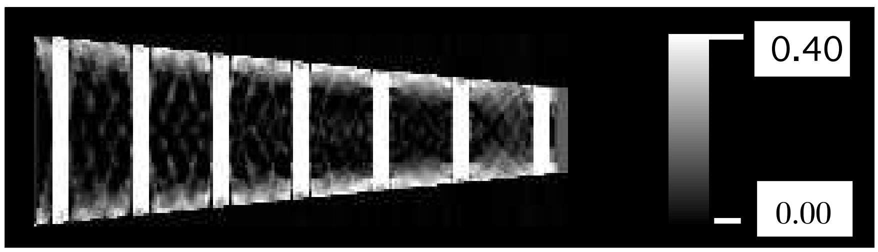

(b)

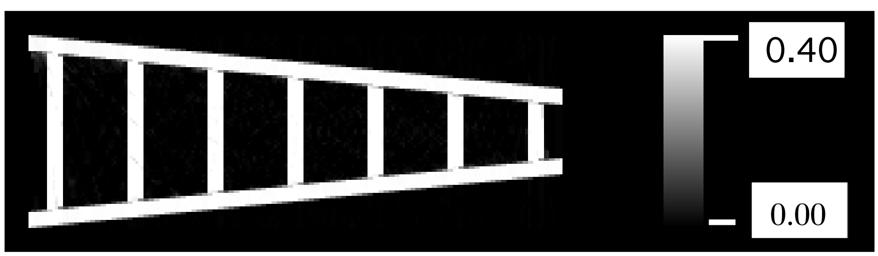

(c)

Fig. 11: Reconstructed images from POCS synthetic data trials: (a) ray sum only, (b) ray sum and spatial support, and (c) ray sum, spatial support and face sheet.

Trial Number	Description	Parameters	Iterations	Error Measure e (%)
1	ray sums only	ε_R=0.001 ε_F=0.1 stop at $\|\mathbf{x}_i - \mathbf{x}_{i-1}\| < 0.1$	13	62.6
2	ray sums and spatial support	ε_R=0.001 ε_F=0.1 stop at $\|\mathbf{x}_i - \mathbf{x}_{i-1}\| < 0.1$	33	38.9
3	ray sums, spatial support, and face sheets	ε_R=0.001 ε_F=0.1 stop at $\|\mathbf{x}_i - \mathbf{x}_{i-1}\| < 0.1$	9	6.0

Table 1: Results for synthetic data trials.

5.4. Real Data Trials

Real data come from measurements of a plexiglass phantom simulating a sandwich structure with graphite/epoxy composite face sheets and aluminum honeycomb core. To avoid resolution problems arising from the thin honeycomb core, components of the phantom are thicker than what is actually found in real aluminum structures. Figure 12 shows schematically the cross section of the plexiglass phantom.

Figure 13 shows the apparatus for ray sum data acquisition. The basis for the apparatus is a real-time radiography system designed for inspecting aircraft control surfaces. The x-ray tube and linear array are mounted on a C-arm manipulator system, allowing the source and sensor to maneuver about and inspect various aircraft parts. The linear array detector is 1024 elements across with an inter-element spacing of 0.2 mm and a width of 0.5 mm. Analog to digital converters digitize the intensity data to 12 bits but at present the frame buffer uses only the eight most significant bits. The frame buffer produces an RS-170 video signal to display images on a video monitor. A PC-based video frame grabber acquires digital data by sampling the frame buffer RS-170 output.

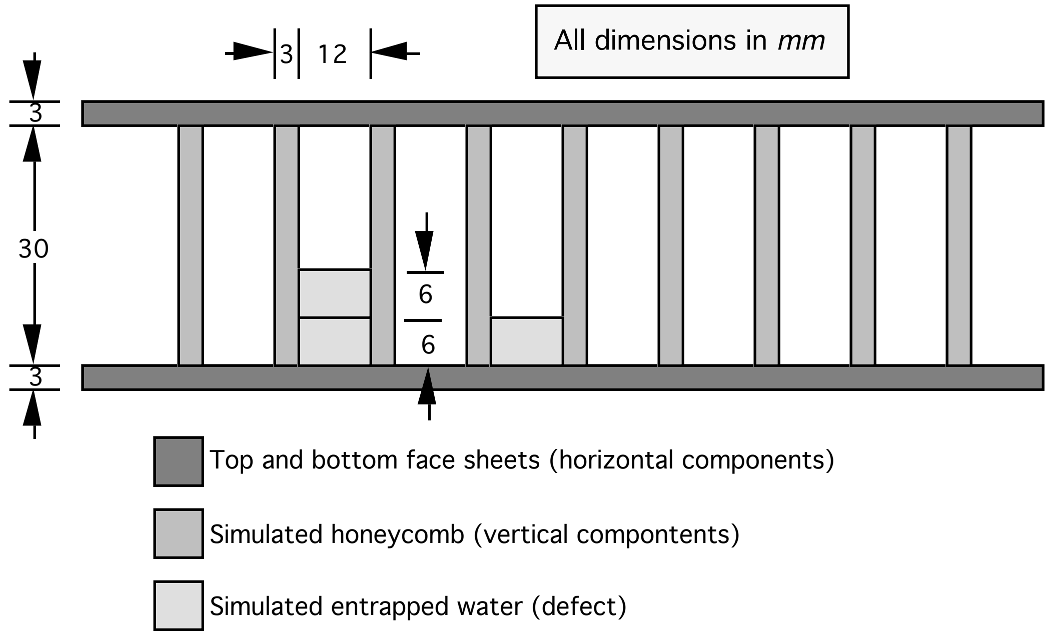

Fig. 12: Cross section of plexiglass phantom simulating a sandwich structure with graphite/epoxy composite face sheets and aluminum honeycomb core.

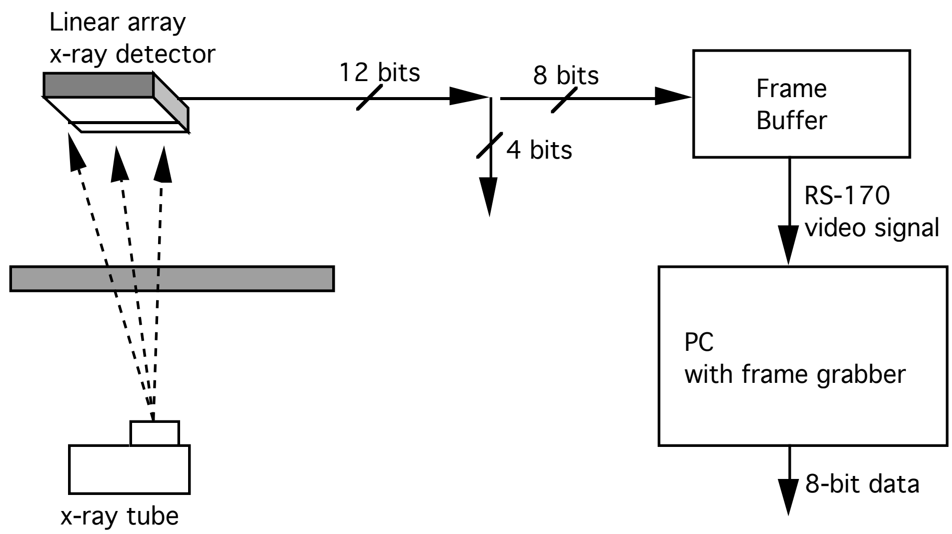

Fig. 13: Apparatus for limited-angle CT ray sum data acquisition system.

The experimental trials use the following procedure to acquire ray sum data:

1. sweep the *C*-arm across the specimen at a constant angle to the specimen and acquire data at 0.5 *mm* interval spacing,

2. with the frame buffer, assemble the data into an image,
3. digitize the image with the PC-based frame grabber,
4. compute the average of the center column of the digitized image and the two columns adjacent to it (to compensate for anomalies created by the linear array), and
5. use the data from the averaged column as a set of parallel ray sums.

There is a variety of error sources inherent in the apparatus. There is no filtration of the x-ray radiation other than that inherent in the manufacture of the tube, so beam hardening is a problem. The linear array requires only a fan of radiation, so any excess radiation contributes to scatter.

The region reconstructed in experiments is 72 rows by 200 columns which, at a resolution of $0.5\,mm$ by $0.5\,mm$, corresponds to a specimen $36\,mm$ thick and $100\,mm$ wide. The plexiglass phantom is $36\,mm$ thick so no pixels in the reconstruction are external to the specimen. As for the synthetic data trials, this trial uses ray sum data for angles from -60° to +60° in steps of 10°. The region of reconstruction precisely matches the spatial support of the specimen so, for this experiment only, it is not necessary to acquire range data. The design of the phantom allows face sheet thickness measurement directly with a micrometer, so thickness ultrasound measurement is not necessary. The $3\,mm$ face sheet thickness (as measured by the micrometer) translates to 6 *pixels*. Therefore, for this trial, the region of known linear attenuation consists of the top and bottom six rows of the reconstruction. The linear attenuation for these rows is that of plexiglass. At the x-ray tube setting of $60\,kV$ used for these experiments, the linear attenuation coefficient of plexiglass is $0.45\,cm^{-1}$.

Figure 14(a) shows the reconstruction of the phantom. Parameters for the reconstruction are $\varepsilon_R = 0.01$ and $\varepsilon_F = 0.1$. With a stopping condition of $\|\mathbf{x}_i - \mathbf{x}_{i-1}\| < 0.1$ the trial requires 30 iterations. Structural detail is clearly visible but there are some artifacts present in the interior of the reconstruction. These artifacts are an inevitable consequence of measurement errors. Although practical application requires better reconstructions, the results show that if the errors are reduced, a sharp accurate reconstruction is possible. Figure 14(b) shows the reconstruction without the use of face sheet constraints. All definition of the face sheets is lost. The fact that the size of the object exactly matches the image enforces the spatial constraints and, consequently, we cannot show an example based on ray sums alone.

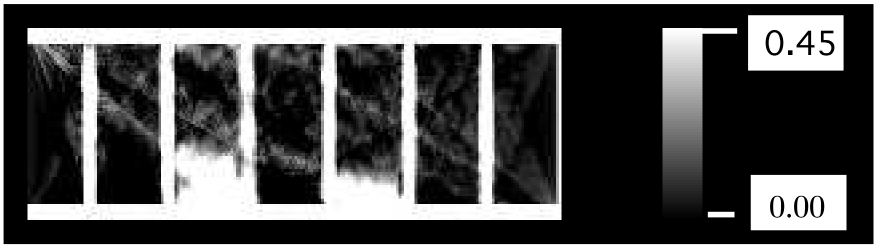

(a)

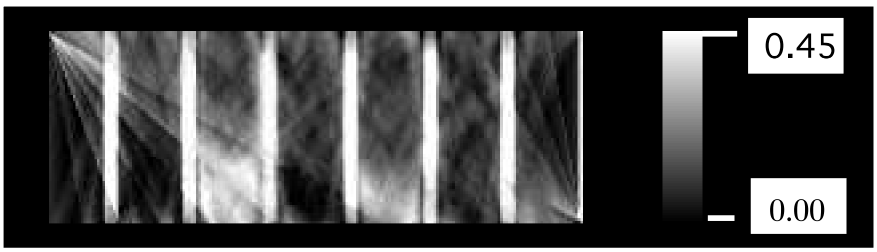

(b)

Fig. 14: Reconstructed cross section of plexiglass phantom: (a) with face sheet constraints, and (b) without face sheet constraints.

6. CONCLUSIONS

Limited-angle CT is an ill-posed problem; more ill-posed than conventional CT. The large null space necessitates the use of *a priori* assumptions to constrain the solution. Unfortunately, the null space includes the face sheets of sandwich structures, rendering the face sheets invisible to ray sum data and confounding reconstruction. For this reason, current limited-angle techniques are unable to reconstruct sandwich structures accurately.

We describe a novel system for limited-angle CT that uses data fusion to accurately reconstruct sandwich structures from limited-angle ray sum data. Additional data from spatial support and face sheet thickness measurements supply constraints to the tomographic reconstruction. Whereas the *a priori* assumptions normally used to constrain reconstruction can be, and are in the case of sandwich structures, invalid, the data fusion constraints are, by nature, consistent with the specimen. Thus, the fusion constraints serve to reduce the null space in a manner consistent with the specimen and lead to accurate reconstructions where otherwise impossible.

The fusion system requires solution of a system of linear equations. We use the method of convex projections, a superset of ART, for a variety of reasons including:

1. it is fast for this problem, and
2. it allows easy combination of differing types of fit to the data.

Other possible methods are singular value decomposition (for small systems), and regularization with quadratic optimization.

Experimental results demonstrate the marked improvement in accuracy with the inclusion of fusion data. Also, real data results show effective application to a real structure. The method gives limited-angle CT the potential for effective application to aircraft control surfaces and similar structures.

ACKNOWLEDGMENTS

The author wishes to thank Bill Ramsbottom of Galatea Research Inc. for his assistance with data acquisition. John Cornes and Ken McRae at Defence Research Establishment Pacific helped with data acquisition and provided advice on ultrasound measurements. Also, the advice and guidance of Dr. Jim Little at the University of British Columbia, Department of Computer Science, was invaluable.

REFERENCES

[1] Herman, G.T., **Image Reconstruction from Projections: The Fundamentals of Computerized Tomography**, Academic Press, New York, 1980.

[2] Davison, M.E., "The Ill-Conditioned Nature of the Limited Angle Tomography Problem," *SIAM Journal of Applied Mathematics*, Vol. 43, No. 2, pp 428-448, 1983.

[3] Louis, A.K., "Incomplete Data Problems in X-Ray Computerized Tomography," *Numerische Mathematik*, Vol. 48, pp 251-262, 1986.

[4] Clark, J.J. and Yuille, A.L., **Data Fusion for Sensory Information Processing Systems**, Kluwer Academic Publishers, Boston, 1990.

[5] Boyd, J.E. and Little, J.J., "Complementary Data Fusion for Limited-Angle Tomography," *CVPR '94,* June 20-23, Seattle, Washington, 1994.

[6] Scudder, H. J., "Introduction to Computer Aided Tomography", *Proceedings of the IEEE,* Vol. 66, No. 6, pp 628-637, 1978.

[7] Tuy, H., "Reconstruction of a Three-Dimensional Object from a Limited Range of Views," *Journal of Mathematical Analysis and Applications*, Vol. 80, pp 598-616, 1981.

[8] Dusaussoy, N.J. and Abdou, I.E., "The Extended MENT Algorithm: A Maximum Entropy Type Algorithm Using Prior Knowledge for Computerized Tomography," *IEEE Transactions on Signal Processing*, Vol. 39, No. 5, pp 1164-1180, 1991.

[9] Grünbaum, F.A., "A Study of Fourier Space Methods for Limited Angle Image Reconstruction," *Numer. Funct. Anal. and Optimiz.*, Vol. 2, No. 1, pp 31-42, 1980.

[10] Tam, K.C., Eberhard, J.W. and Mitchell, K.W., "Incomplete-Data CT Image Reconstructions in Industrial Applications," *IEEE Transactions on Nuclear Science*, Vol. 37, No. 3, pp 1490-1499, 1990.

[11] Heiskanen, K.A., Rhim, H.C. and Monteiro, J.M., "Computer Simulations of Limited Angle Tomography of Reinforced Concrete," *Cement and Concrete Research*, Vol. 21, pp 625-634, 1991.

[12] Soumekh, M., "Image Reconstruction from Limited Projections using the Angular Periodicity of the Fourier Transform of the Radon Transforms of an Object," *Acoustical Imaging*, Vol. 13, Proceedings of the Thirteenth International Symposium, Minneapolis, MN, USA, pp 31-42, October 1983.

[13] Boyd, J.E., "A Novel Constraint-Based Data Fusion System for Limited-Angle Computed Tomography," University of British Columbia, Department of Computer Science Technical Report, No. TR94-7, March 1994.

[14] Brègman, L.M., "The Method of Successive Projection for Finding a Common Point of Convex Sets," translated by J.G. Ceder, *Doklady*, Vol. 162, No. 3, pp 688-692, 1965.

[15] Youla, D.C. and Webb, H., "Image Restoration by the Method of Convex Projections: Part 1 - Theory," *IEEE Transactions on Medical Imaging*, Vol. MI-1, No. 2, October 1982.

[16] Gubin, L.G., Polyak, B.T., and Raik, E.V., "The Method of Projections for Finding the Common Point of Convex Sets." *U.S.S.R Computational Mathematics and Mathematical Physics*, Vol. 7, No. 6, pp 1-24, 1967.

[17] Bauschke, H.H. and Borwein, J.M., "On Projection Algorithms for Solving Convex Feasibility Problems," Simon Fraser University, Department of Mathematics and Statistics Research Report No. 93-12, Burnaby, British Columbia, Canada, 1993.

[18] Censor, Y. and Herman, G.T., "Row-Generation Methods for Feasibility and Optimization Problems Involving Sparse Matrices and Their Applications," *Sparse Matrix Proceedings* 1978, SIAM, Philadelphia, pp 197-219, 1978.

[19] Trummer, M.R., "A Note on the ART of Relaxation," *Computing*, Vol. 33, pp 349-352, 1984.

[20] Oskoui-Fard, P, and Stark, H., "Tomographic Image Reconstruction Using the Theory of Convex Projections," *IEEE Transactions on Medical Imaging*, Vol. 7, No. 1, March 1988.

[21] Oskoui-Fard, P, and Stark, H., "A Comparative Study of Three Reconstruction Methods for a Limited-View Computer Tomography Problem," *IEEE Transactions on Medical Imaging*, Vol. 8, No. 1, March 1989.